Article

Modelling the Growth and Aggregation of Gold Nanoparticles Using Liquid-Phase Transmission Electron Microscopy

Thao Ngo, Siying Yu, and Hong Yang *

Department of Chemical and Biomolecular Engineering, University of Illinois Urbana-Champaign, 206 Roger Adams Laboratory, 600 South Mathews Avenue, Urbana, IL 61801, USA
* Correspondence: hy66@illinois.edu
Received: 2 August 2024; Revised: 5 June 2025; Accepted: 8 June 2025; Published: 18 June 2025

Abstract: The ability to synthesize nanoparticles of desired shape, size and composition relies heavily on our understanding on how to finely control various factors influencing the formation, such as the kinetics of growth. Fundamental study on the nucleation and growth of nanoparticles found itself at the forefront with the application of liquid-phase transmission electron microscopy (LTEM) in the investigation of dynamic growth and assembly processes. Since early study using LTEM to observe and quantify the nucleation and growth of single colloidal platinum nanoparticles, several theoretical models have been developed. More complex mode of formation was also revealed based on a hybrid growth process of gold on platinum icosahedral nanoparticles to form core-shell structures. These studies have been carried out by focusing on single or a small number of nanoparticles. Herewith, we present a study on the establishment of an analytical method to quantify the particle formation using in situ LTEM technique. This approach is based on the analysis of median particle size and focused on main events accounted for the formation of nanoparticles at a given time. We found that unlike the cases for single particle analysis, the observed formation rate could not be explained by any single formation mode, such as diffusion- and/or reaction-controlled growth described by the Liftshitz-Slyosov-Wagner theory or formation through coalescence as described by the Smoluchowski aggregative kinetics. A global fit was used to describe the entire formation of nanoparticles in an ensemble.

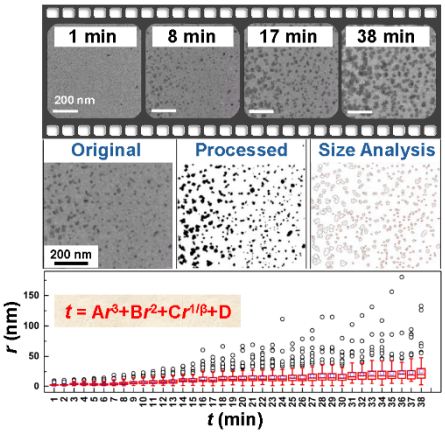

Keywords: LTEM; modelling; nanoparticle; growth; aggregation

1. Introduction

Nanomaterials are important in various fields including catalysis, biomedicine, gas sensing, and magnetic data storage, just to name a few, because of their unique properties, which arise from size- and shape-related properties [1–8]. It is essential that the formation of well-controlled nanoparticles can be quantitatively understood through the analysis of data obtained in reaction media throughout the various stages of formation [9–11]. Transmission electron microscopy (TEM) has been the method of choice for studying the kinetics and formation mechanisms of nanoparticles, such as growth and dissolution of colloidal nanocrystals. Prior to the invention of liquid-phase TEM (LTEM), a commonly used strategy for obtaining information regarding growth is to examine samples taken out from solutions at predetermined time points using TEM imaging [12–14]. This method, however, has the intrinsic uncertainty on whether ex situ data can offer an accurate picture of the formation in solution.

In this regard, LTEM is a powerful tool to investigate the formation of nanoparticles through various dynamic processes, such as growth and attachment in reaction media [15–24]. Noticeably, LTEM has been used to quantify the growth rate of colloidal Pt nanocrystals [25], Pt_3Fe nanorods [16], and core-shell nanostructures [26–28]. LTEM is also instrumental in revealing details of complex growth processes such as hybrid growth and subsequent surface diffusion [28,29], oriented attachment [9,30–33], self-assembly [34,35], and formation of superlattices and

supracrystals [36–38]. LTEM studies have not only furthered the development of existing theories, but also uncovered new growth processes that do not strictly adhere to those classical models of nucleation and growth based largely on precipitation phenomena [39–42].

The majority of LTEM studies on the formation of nanoparticles have so far focused on single or few nanoparticles without giving the much-needed consideration of the dynamics of nanoparticle formation as an ensemble [24,43,44]. While it is extremely useful in understanding the growth [45], the current approach does not entirely encompass the formation of nanoparticles in a solution containing a population of polydisperse nanoparticles at various growing stages, herein referred to as an ensemble, which is the most common case. For an ensemble, coalescence is yet another major factor for the formation of nanoparticles, besides the nucleation and growth from monomers [46,47]. Therefore, there is a clear need to develop methods to describe the formation by taking into consideration of both individual nanoparticle and ensemble in a solution environment.

Previously, it was shown by in situ LTEM the rate of formation of hybrid organic-inorganic perovskite nanoparticles did not follow either diffusion- or reaction-limited growth model as predicted by the Liftshitz-Slyosov-Wagner (LSW) theory [44]. Non-classical growth modes involving aggregation and coalescence were reported to be responsible for the formation of Au nanoparticles in an ensemble [43]. Quantitative analysis on particle size reveals that although the rate of growth follows that explained by the classical LSW theory, particle size distribution follows the model described by Smoluchowski aggregative kinetics [43]. In this study, we present a new method to quantify the formation of the whole formation of Au nanoparticles, including both the growth and ensemble, through mathematical fitting of particle size and size distribution. The data obtained through in situ LTEM are used to analyze the possible contributions of major driving forces for the formation of nanoparticles, that is, diffusion, surface reaction, and particle coalescence. We show that no single formation factor can be used to fit the entire experimental data obtained for an ensemble of Au nanoparticles formed under different conditions in a spatiotemporal analysis. Instead, the formation rate can be in both diffusion- and reaction-controlled regime in the early stages, while the coalescence-controlled regime is too complicated to be interpreted by the classical models.

2. Experimental Section

2.1 In Situ Growth of Au Nanoparticles

The solution mixture for the synthesis was made of 0.1 M tetrachloroauric acid ($HAuCl_4$, Sigma-Alrich (St. Louis, MO, USA), 99.995% trace metal basis) prepared by dissolving its hydrated form in deionized water (DI, H_2O). A droplet of the growth solution was placed in a liquid cell made of two 50 nm thick silicon nitride (SiN) windows supported on Si wafers separated by a 250-nm thick spacer (Figure 1). First, the spacer chip was placed into its slot in the tip of the LTEM holder (Hummingbird Scientific, Lacey, WA, USA), followed by the placement of a 2-μL droplet of 0.1 M $HAuCl_4$. The top chip was then carefully positioned atop the droplet of growth solution. A toothpick was used to gently press the top chip down so that the droplet spread out and to align the SiN windows. Once the windows were aligned, the cell was closed and tested for vacuum leakage using an external vacuum pump. Upon achieving a desirable pressure in the order of 10^{-6} bar, which is an indication of a well-sealed cell, the liquid cell was inserted into a TEM (Hitachi 9500, Hitachi High-Tech., Schaumburg, IL, USA) for study.

Au nanoparticles formed under the electron beam that was also used for the imaging of the growth process inside the liquid cell in TEM. The growth of Au nanoparticles was recorded at a beam current density of 8×10^{-12} A/cm^2 and magnification of ×12,000, corresponding to a constant electron dosage of 0.727 electron per Å^2 per second (e^-/(Å^2·s)). The typical total recording time was 40 min, after which no further changes were observed. The electron beam was kept on the imaging area for the entire duration of in-situ study.

2.2 Image Analysis

Still frames of 1 min apart each were obtained from the recorded in situ video of LTEM study. ImageJ software was used to count and measure the sizes of Au nanoparticles over time. By utilizing the difference in contrast between the nanoparticles and the surrounding solution, outlines of the nanoparticles in each frame were extracted (Figure 2). ImageJ was then used to measure the projected area of the nanoparticle. To comparing the formation rate of these nanoparticles over time with the growth rate predicted by LSW theory, the areas were converted to radius according to the equation, $A = \pi r^2$, where A is the projected area of the particle and r is the calculated radius. Particle overlapping can be an issue when the density of particles is high, especially at the later stage of particle growth. Thus, we only applied the proposed analysis to frames obtained from the very beginning till the time when particle overlapping became significant (i.e., 38 min in this study). Overlapped particles

exhibited dark color and were distinguishable from non-overlapping ones in our TEM micrographs, which all had relatively clean backgrounds.

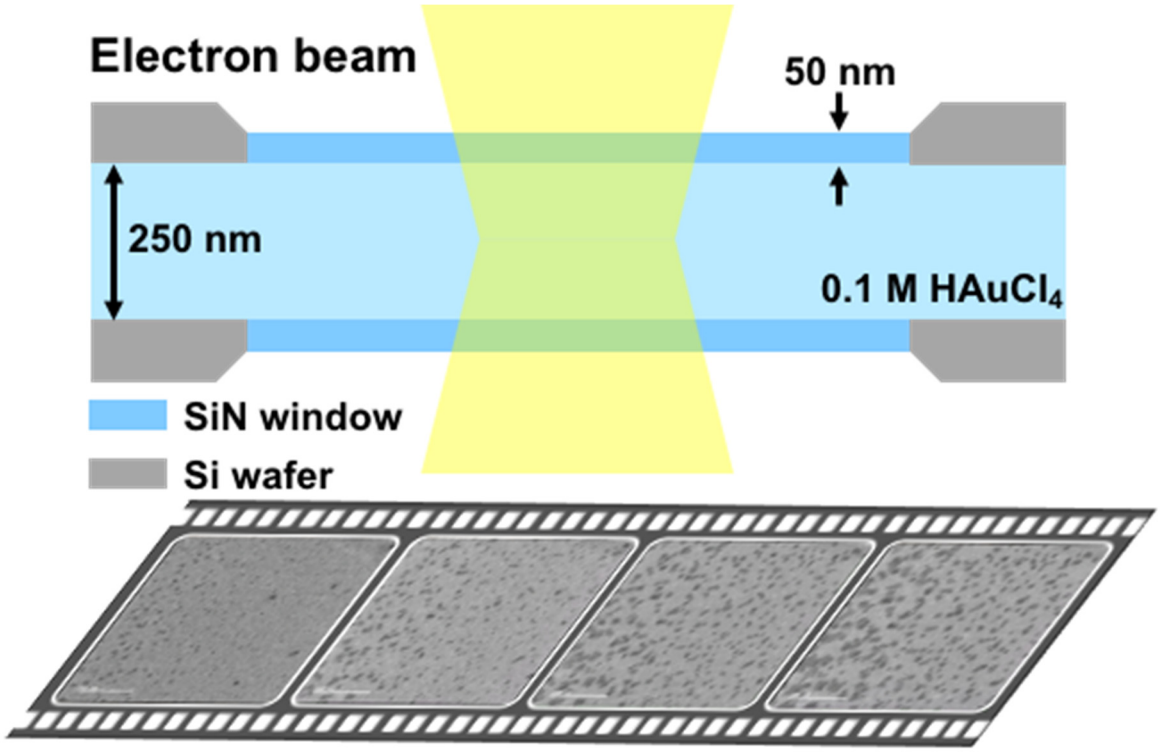

Figure 1. Illustration of the liquid cell for TEM used in this study. The scale bars in the micrographs are 200 nm.

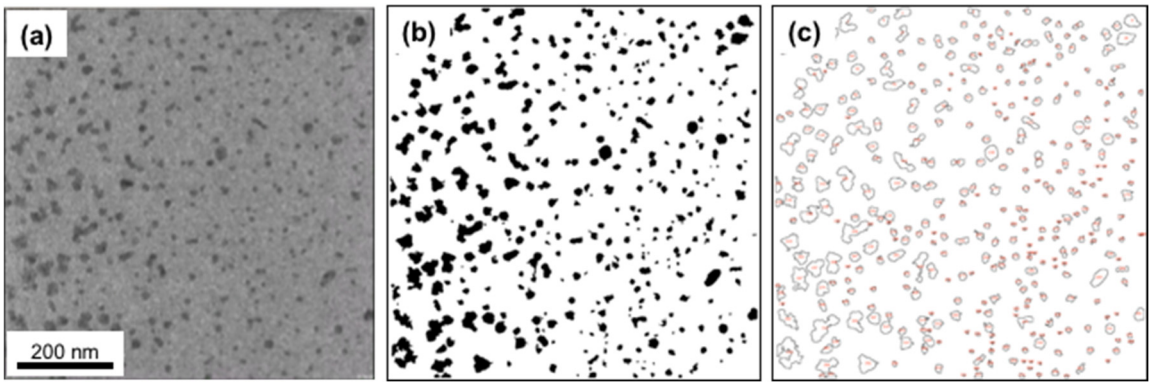

Figure 2. Illustration of the analysis of particle number and size from a LTEM micrograph using ImageJ software. (**a**) Still frame extracted from the LTEM video recorded during the growth, (**b**) processed image based on the contrast, and (**c**) image showing the outlines of the counted nanoparticles.

3. Results and Discussion

Figure 3 shows an ensemble of Au nanoparticles formed over a period of 38 min in an aqueous solution inside a TEM liquid cell at a dose rate of 0.727 $e^{-}/(Å^2 \cdot s)$. This rate of irradiation is significantly lower than the typically imaging condition, i.e., 5~50 $e^{-}/(Å^2 \cdot s)$ [48–50], thus the dendritic growth of Au particles was efficiently suppressed at the onset of the process [28]. Both the number and size of particles grew over time. The nanoparticles forming at the initial stages tend to be spherical in shape but became faceted and irregular in shape over the time of the recording period [51].

In the first 20 min, these nanoparticles grew both by the addition of monomer and later through the interactions among neighboring particles (Figure 4). Two types of particle interactions were observed from 8 to 20 min: the consumption of small particles by large ones (i.e., Ostwald ripening) and the coalescence of nanoparticles of similar sizes. Toward the end of recording, dendritic growth, which appeared to be suppressed to some extent, could however still be observed even though the dose rate was kept at a low level. It is likely the solvated electrons generated by the interaction between the electron beam and the aqueous solution was able to

accumulate over time till eventually establishing a steady state, because the experiments were carried out under the static environment [52]. In addition, the last two images recorded at 36 and 38 min were noticeably brighter in contrast than the others, suggesting a decrease in the thickness of liquid layer (Figure 3). The accumulation of solvated electrons and thinning of liquid thickness likely caused the formation of dendrites.

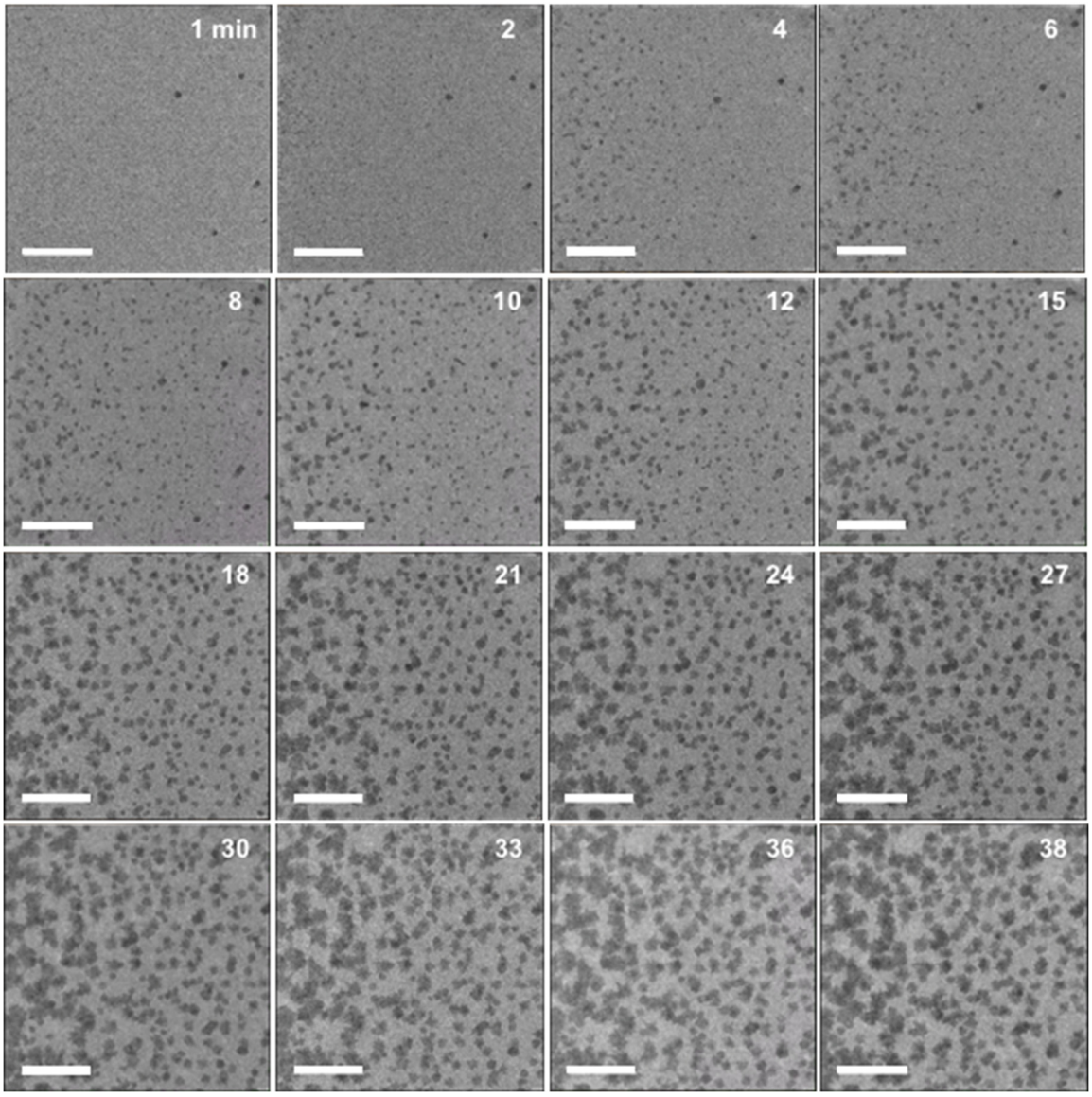

Figure 3. Still images extracted from in situ LTEM video of the formation of an ensemble of Au nanoparticles over the given times in minutes (at the top right of each TEM micrograph). The scale bars are 200 nm.

Figure 5 shows the quantitative analysis of number of nanoparticles formed using ImageJ software. The formation could be divided into three stages, as determined by the rate of change in the number of nanoparticles (n_s) and particle size over time (t), which is the slope of the linear function between n_s and t (Figure 5a). In Stage I, nanoparticles grew rapidly at a rate of ~59 particles/min, apparently via monomer addition, up to about 6 min. During Stage II, the total number of nanoparticles decreased with time at a rate of 23 particles/min. In Stage III, the combination of neighboring particles slowed down, as indicated by a decrease in the rate of change of n_s over t to 6.6 particles/min from 23 particles/min in Stage II. The main mode of formation at this stage was dendritic growth from the existing particles with some combination of particles, judging by the TEM images. No major changes in n_s and particle size were observed after reaction time reached 38 min, as shown in Figure 3.

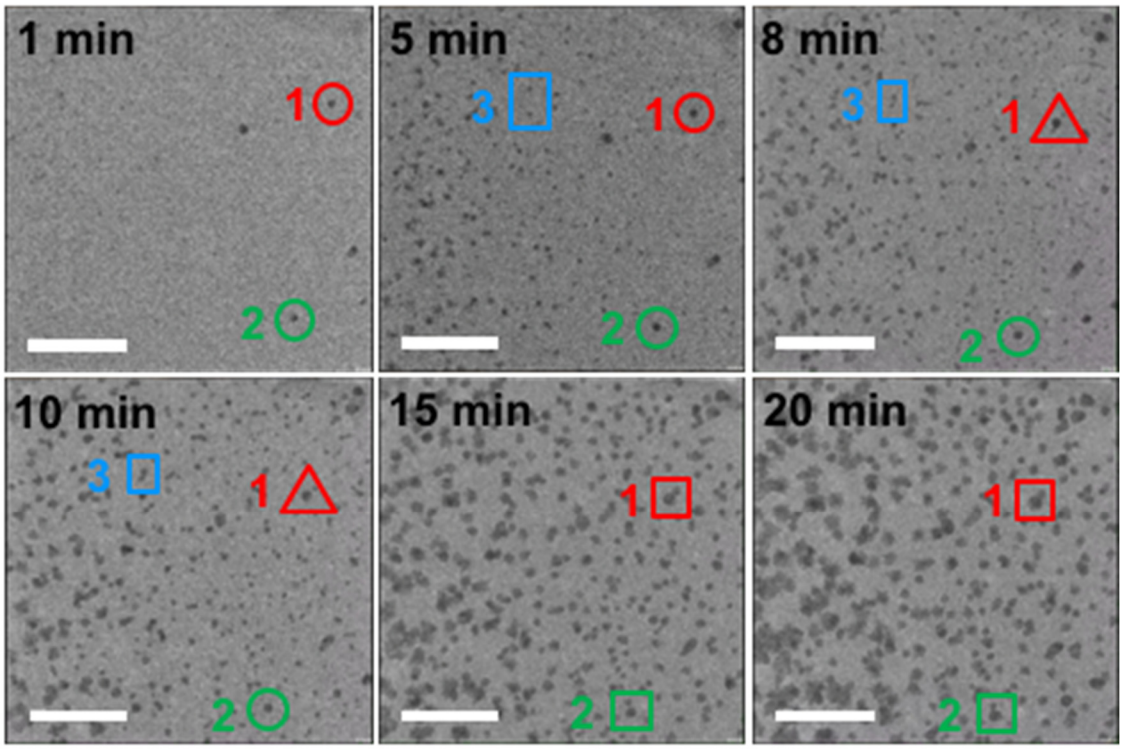

Figure 4. TEM images showing the formation of three Au nanoparticles via monomer addition (circle), coalescence (square), and Ostwald ripening (triangle). Same color is used to follow the same particle. The scale bars are 200 nm.

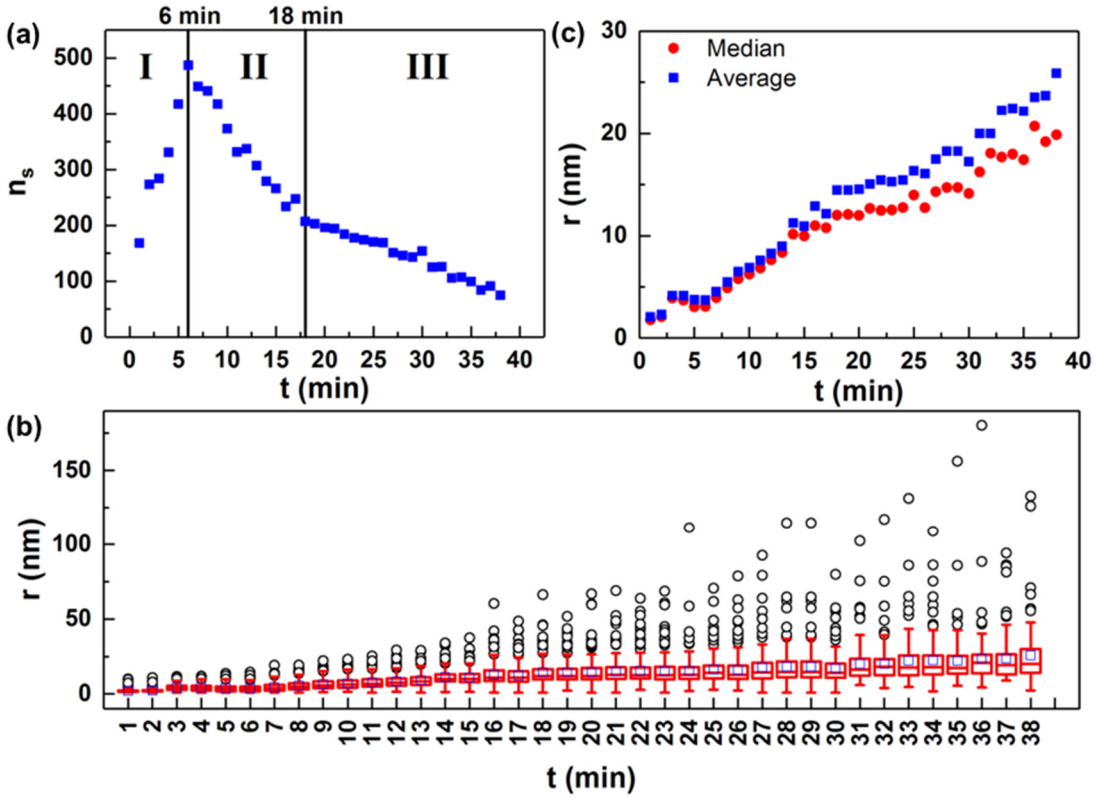

Figure 5. Changes of number and size of particles extracted from in situ LTEM data. (**a**) Number of particles (n_s,) as a function of time (t). (**b**) Particle size (r) over time (t) in the form of a box plot with outliers. The line and blue square inside each box represent the median and average particle size at that time, respectively. The top of the box represents the upper quartile while the bottom of the box represents the lower quartile. The upper and lower whiskers represent particles with sizes that fall outside the middle 50%. (**c**) Median and average particle size as a function of time extracted from (**b**).

One challenge on analyzing ensemble data from the LTEM is the heterogeneity of the nanoparticle formed under rather complex reaction conditions due to the electron beam irradiation of static nature of the cell [53]. Thus, it was important to perform a statistical analysis to determine the data set to be used prior to the fitting of experimental data. Particularly, it is necessary to determine whether to choose the average or median radii for the particle size. As shown in Figure 5b, as time increased, the variation in size increased. Furthermore, the average radii were deviated greatly from the median at some time points (Figure 5c). Our study indicates based on the statistical analysis, median radii could be the representative values to analyze the rate of formation based on majority of the particle population in the ensemble and were used for the data analysis.

Based on the data set obtained through the above statically analysis of median radii, we quantified the formation of nanoparticles by considering main controlling factors, including diffusion, reaction, and particle coalescence both individually and in a global analysis. For the growth, we turned to the classical LSW theory, which considers the nanoparticle growth a solution in two major steps: diffusion of monomers from the bulk solution onto the surface of a seed, and reaction of monomers at the surface [54]. Equation (1) gives the general expression describing the size evolution of a single nanoparticle (a detailed derivation of Equation (1) based on the Fick's first law is presented in the Supporting Information):

$$\frac{dr}{dt} = \frac{2\gamma V_m^2 C_\infty}{RT(1/D + 1/k_d r)} \frac{1/r_b - 1/r}{r} \tag{1}$$

where r is the radius, r_b is the distance from the bulk to the center of the particle, γ is the interfacial energy, V_m is the molar volume, C_∞ is the concentration of a flat particle, R is the gas constant, T is temperature, D is the diffusion coefficient, and k_d is the rate constant. In the case of a diffusion-limited growth that the particle size is controlled by the diffusion of the monomers to the surface Equation (1) is reduced to the following form:

$$\frac{dr}{dt} = \frac{2\gamma D V_m^2 C_\infty}{RT} \frac{(r/r_b - 1)}{r^2} \tag{2}$$

Given that the total mass of the system is conserved, the LSW theory shows that the ratio r/r_b is a constant; Equation (2) can further be simplified to

$$\frac{dr}{dt} = K_D \frac{1}{r^2} \tag{3}$$

Equation (3) can be solved to obtain the time-dependent expression for particle size:

$$r^3 - r_0^3 = K_D t \tag{4}$$

where r_0 is the median radius of the particle at time $t = 0$, and K_D is a coefficient leading t and is given by the following expression:

$$K_D = \frac{8\gamma D V_m^2 C_\infty}{9RT} \tag{5}$$

For the growth of particle controlled by reactions of monomers at a surface of a particle, Equation (1) is reduced to the following form:

$$\frac{dr}{dt} = \frac{2\gamma k_d V_m^2 C_\infty}{RT} \frac{(r/r_b - 1)}{r} \tag{6}$$

Similar to the diffusion-controlled growth, the ratio r/r_b remains constant if the total mass of the system is conserved. Integrating Equation (6) yields the relationship between particle size and time for the case of a reaction-controlled growth:

$$r^2 \approx K_R t \tag{7}$$

The obtained radii of the nanoparticles were fit with the above equation (Figure 6). Neither the diffusion- nor reaction-controlled case derived from LSW theory could fit the experimental data of the relationship between particle size and time over the entire period. For particle formation under this experimental condition, the initial formation was indeed influenced mainly by both the diffusion of monomers and surface reaction, as shown by a reasonable fit using the LSW theory to the experimental data within the first 6 min or so (Figure 6) [45,55].

The deviation from the experimental data based on the LSW theory stems from the formation dominated by modes other than growth, that is, particle coalescence in the ensemble. One approach is to include new terms to the existing fit to account for the formation through both monomer growth and particle coalescence. In another

word, the formation through coalescence can be factored into the fit describing only the growth. We hypothesized effect of coagulation should be included to fit the curve of size evolution over time when particle aggregated [56].

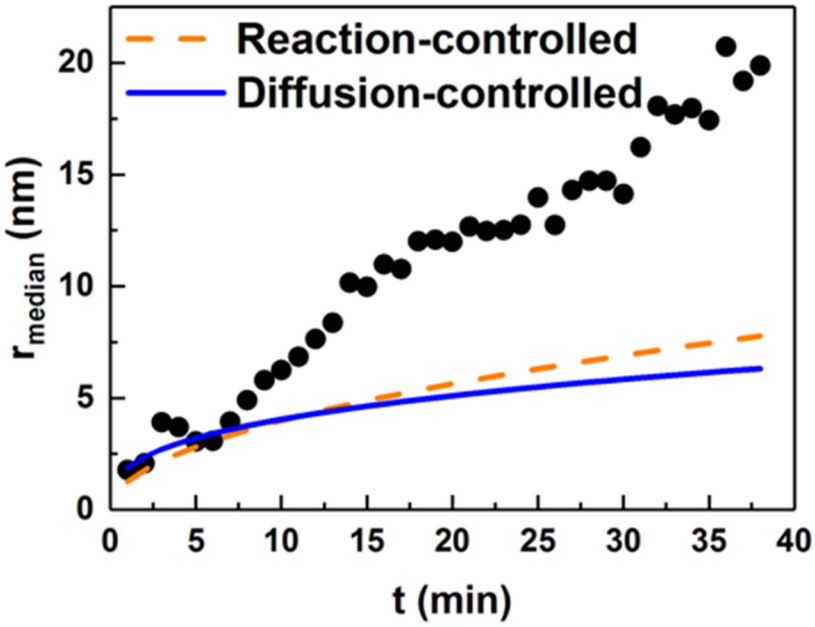

Figure 6. Experimental data and theoretical fits of median particle size as a function of time using expressions describing reaction- and diffusion-controlled growth by LSW theory.

The necessity to incorporate both LSW theory and coagulation kinetics was analyzed based on particle size distribution (PSD) of the samples. As shown in Figure S1, PSD is obtained by normalizing the radii of nanoparticles in each time frame to the respective mean nanoparticle radius at that time. The normalized radii are then normalized to the total integral to gain the frequency. To compare experimental data with existing theories, PSD predicted by LSW theory and Smoluchowski aggregation kinetics were included. The expressions and derivation for theorical PSD can be found in the SI. As can be seen in Figure S1, the PSD extracted from the growth of nanoparticles did not follow those predicted by either LSW or Smoluchowski theories. The experimental PSD is observably more symmetric compared to theoretical PSD curves in general. For the first stage of growth (stage I), the PSD decreased in magnitude and shifted to the left, as indicated by the red arrow. Based on the PSD predicted by the LSW theory and the Smoluchowski coalescence kinetics, the changes in the PSD for the first 6 min reflected a shift from growth via mixed diffusion- and reaction-limited regime toward growth via coalescence. During the second stage of growth (stage II), PSD shifts from right to left with an increase in magnitude, suggesting a shift in the mode of formation. In this study nanoparticles could freely move to coalesce to reduce surface energy because there was no surfactant used. After the movable nanoparticles exhausted, the ensemble reverted to the growing mode via monomer addition. In the last stage of growth (stage III), the PSD determined experimentally showed little change in terms of shift in relative size and magnitude in frequency.

It is worthwhile to note that during the last stage of growth, nanoparticles continued to grow via the formation of dendrites. The formation of dendrites is characteristic of a kinetic-controlled process and highly sensitive to the monomer supersaturation level in the growth solution. Dendrites tend to form under high supersaturation conditions and evaporation time of the aqueous precursor solution. Oversaturation (S) was calculated and plotted against time (t) in Figure S2 using experimental growth rate, based on the relationship between critical radius (r_{cr}) [45]:

$$r_{cr} = \frac{2\gamma V_m}{RT \ln S} \tag{8}$$

Figure S2 shows that oversaturation decreased rapidly over time because of monomer consumption during the growth process. Other factors may include evaporation or thinning of the liquid layer, as evidenced by the change to lighter contrast of the background at the later stages of formation of particles (as shown in the inset of Figure S2) or movement of the liquid within the cell, causing oversaturation to be much higher than expected and subsequent formation of dendrite.

Evolution of an ensemble of nanoparticles was previously examined theoretically using Monte Carlo simulation [45]. The obtained rate from the simulation was much higher than that predicted by the LSW theory,

but similar to the rate obtained experimentally in this study. A solution thus is to include an additional parameter to the two-term expansion of the Gibbs-Thompson equation in the followings:

$$\frac{dr}{dt} = \frac{2K'\gamma V_m^2 C_\infty}{RTr^2(1/D + 1/k_d r)} \tag{9}$$

Equation (9) can be rearranged to

$$\frac{RT}{2DK'\gamma V_m^2 C_\infty} r^2 dr + \frac{RT}{2k_d K'\gamma V_m^2 C_\infty} r dr = dt \tag{10}$$

which can then be integrated to obtain the following equation for data simulation:

$$Ar^3 + Br^2 + C = t \tag{11}$$

where A is equal to $\frac{RT}{2DK'\gamma V_m^2 C_\infty}$, B is equal to $\frac{RT}{2k_d K'\gamma V_m^2 C_\infty}$, and C is a constant. This treatment considers the intermediate regime in which both diffusion and surface reaction contribute to the growth process and the ratio r/r_b is assumed to be a constant, K'.

Particle growth via coalescence has been analyzed using a power law in the Monte Carlo simulation, $r \sim t^\beta$ [57], where β is the coalescence exponent and a function of a parameter α that describes the nature of the movement of nanoparticles. The relationship between β and α is described by the following expression:

$$\beta = \frac{1}{2(\alpha + 1)} \tag{12}$$

Equation (11) offers an approach via which formation of nanoparticles based on coalescence can be considered by measuring the coalescence exponent. To evaluate what a likely value β could be, we analyzed the changes in size of several individual nanoparticles at the late stages, during which coalescence took place and plotted against time (Figure S3). The radii as a function of time of several nanoparticles were fitted using a power law, $r \sim t^\beta$, and the results for β are shown in Figure 7.

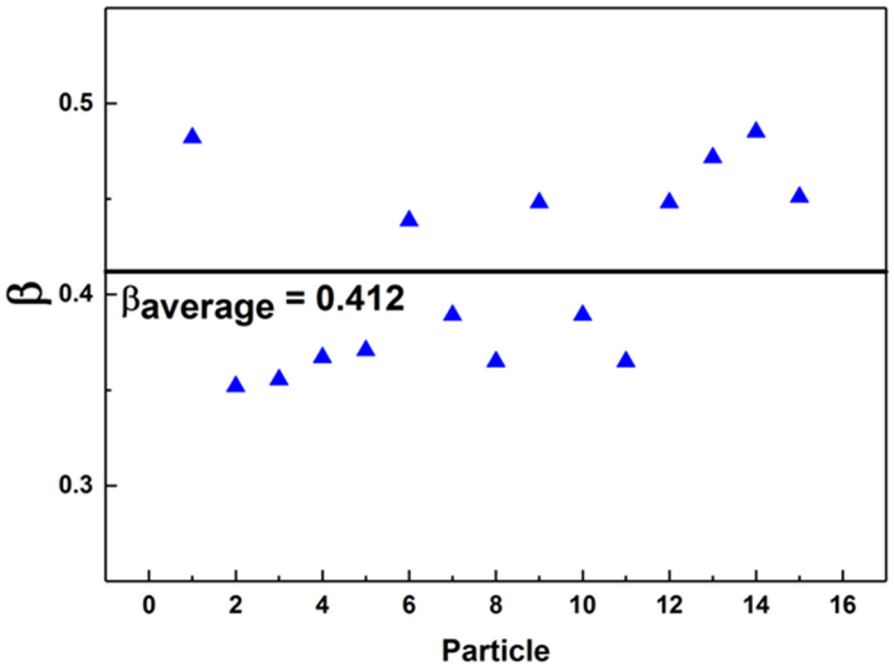

Figure 7. β value obtained from fitting the growth rate of nanoparticles grown via coalescence.

Values for α were typically in the range of $0 < \alpha < 2$, corresponding to β values not to exceed 0.5 [56]. In this study, all of experimentally determined β values met this upper limit. For the analysis, an average value of 0.412 was used for β, corresponding to an α value of 0.214. Thus, to factor in contribution to the particle formation from coalescence, a term corresponding to the particle formation via coalescence in the form of $t \sim r^{1/\beta}$ should be added to Equation (10) to obtain a new form describing the formation of particles in an ensemble in solution through all the stages:

$$t \approx Ar^3 + Br^2 + Cr^{1/\beta} + D \quad (13)$$

We used this new global analysis equation to fit the experimental data for the formation of Au nanoparticles in solution obtained by in situ LTEM (Figure 8). The fitting resulted in the following equation for quantifying the change of particle size over time, $r(t)$:

$$(8.06 \times 10^{-19})r^3 + 0.31r^2 - 0.062r^{2.43} + 1.92 = t \quad (14)$$

where the values of A, B, C and D are 8.06×10^{-19}, 0.31, −0.062, and 1.92, respectively; and β is 0.412. One may use the obtained coefficients and experientials to further examine the various regimes for the particle formation, though the negative value of coefficient C is not understood. For example, in this system the value of A (8.06×10^{-19}) is much smaller than that of B (0.31). This result indicates that under this reaction condition, diffusion is more prominent than surface reaction, because coefficient A is inversely related to the diffusion coefficient, while coefficient B is inversely related to the surface reaction coefficient (k_d).

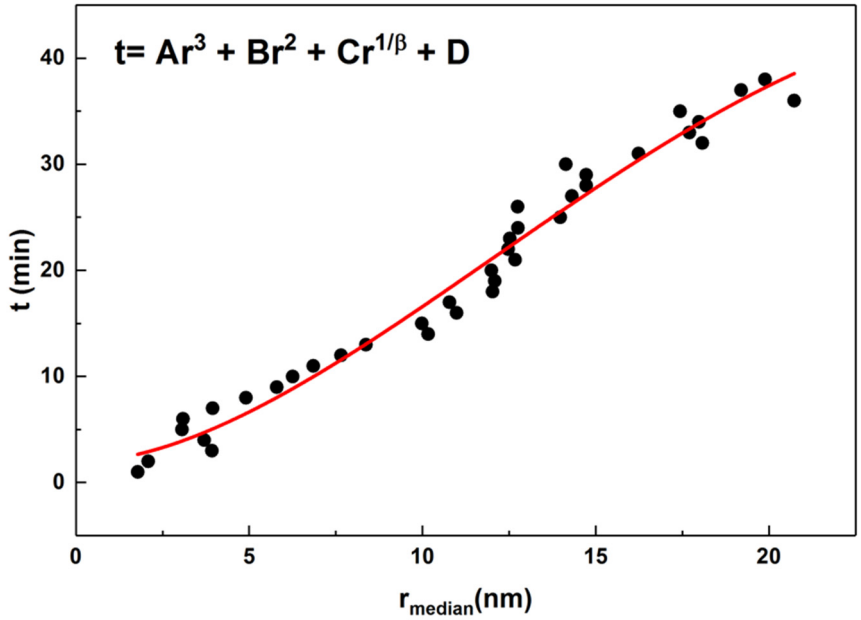

Figure 8. Time (t) as a function of radius (r) and a fit based on Equation (13) aiming at describing the formation of nanoparticles by mixed diffusion- and reaction-controlled growth and particle coalescence (red curve).

4. Conclusions

In this study, the formation of Au nanoparticles was quantitatively analyzed using in situ LTEM. The simulation of the data for the formation was analyzed by considering both LSW theory for nucleation and growth, and coagulation kinetics of an ensemble. No existing treatment could satisfactorily describe the entire formation process observed, and a polynomial expression was developed to fit the diffusion- and reaction-controlled growth and particle coalescence. This approach allows for a description of the complexity in the particle formation for the entire process: the initial monomer addition controlled by both diffusion and surface reaction processes (Stage I); the monomer addition and coalescence (Stage II); and the dendritic formation at the end (Stage III). Using polynomial expression to fit the data could be applicable for simulation of the formation of nanoparticles that go through growth and coagulation in solution, though understanding the insight of the formation is still a challenge.

Supplementary Materials: The following supporting information can be downloaded at: https://media.sciltp.com/articles/others/2506181658399634/MI-439-Supplementary-Materials.pdf, Supplementary notes on derivation of LSW theory and PSD; Figure S1: Particle size distribution (PSD) of the experimental radii compared to those predicted from the LSW theory; Figure S2: Oversaturation (S) as a function of time (t); Figure S3: Analysis of nanoparticles grown via coalescence. Reference [58] is cited in the Supplementary Materials.

Author Contributions: T.N.: Conceptualization, Validation, Methodology, Data Duration, Formal Analysis, Writing-original draft, Writing-review & editing; S.Y.: Writing-review & editing; H.Y.: Conceptualization, Methodology, Writing-review & editing, Supervision, Resources, Investigation, Funding acquisition. All authors have read and agreed to the published version of the manuscript.

Funding: This research was funded by U.S. National Science Foundation (Funding No.: OISE-1515376), and University of Illinois.

Data Availability Statement: Data is available from the corresponding author upon reasonable request.

Acknowledgments: We thank U.S. National Science Foundation (NSF, OISE-1515376) and University of Illinois for support of this research. The electron microscopy study was carried out at Materials Research Laboratory at University of Illinois. T. N. is grateful for a National Science Foundation Graduate Research Fellowship.

Conflicts of Interest: The authors declare no conflict of interest. The funders had no role in the design of the study; in the collection, analyses, or interpretation of data; in the writing of the manuscript; or in the decision to publish the results.

References

1. Lu, J.; Wu, W.; Colombari, F.M.; Jawaid, A.; Seymour, B.; Whisnant, K.; Zhong, X.; Choi, W.; Chalmpes, N.; Lahann, J.; et al. Nano-Achiral Complex Composites for Extreme Polarization Optics. *Nature* **2024**, *630*, 860–865.
2. Boles, M.A.; Ling, D.; Hyeon, T.; Talapin, D.V. The Surface Science of Nanocrystals. *Nat. Mater.* **2016**, *15*, 141–153.
3. Yang, X.; Yang, M.; Pang, B.; Vara, M.; Xia, Y. Gold Nanomaterials at Work in Biomedicine. *Chem. Rev.* **2015**, *115*, 10410–10488.
4. Murphy, C.J.; Vartanian, A.M.; Geiger, F.M.; Hamers, R.J.; Pedersen, J.; Cui, Q.; Haynes, C.L.; Carlson, E.E.; Hernandez, R.; Klaper, R.D.; et al. Biological Responses to Engineered Nanomaterials: Needs for the Next Decade. *ACS Cent. Sci.* **2015**, *1*, 117–123.
5. Wu, J.; Yang, H. Platinum-Based Oxygen Reduction Electrocatalysts. *Acc. Chem. Res.* **2013**, *46*, 1848–1857.
6. Xia, Y.; Yang, P.; Sun, Y.; Wu, Y.; Mayers, B.; Gates, B.; Yin, Y.; Kim, F.; Yan, H. One-Dimensional Nanostructures: Synthesis, Characterization, and Applications. *Adv. Mater.* **2003**, *15*, 353–389.
7. Zhou, L.; Huang, Q.; Xia, Y. Plasmon-Induced Hot Electrons in Nanostructured Materials: Generation, Collection, and Application to Photochemistry. *Chem. Rev.* **2024**, *124*, 8597–8619.
8. Yu, S.; Yang, H. Design Principles for the Synthesis of Platinum–Cobalt Intermetallic Nanoparticles for Electrocatalytic Applications. *Chem. Commun.* **2023**, *59*, 4852–4871.
9. Peng, Z.; You, H.; Yang, H. Composition-Dependent Formation of Platinum Silver Nanowires. *ACS Nano* **2010**, *4*, 1501–1510.
10. Park, J.; Joo, J.; Kwon, S.G.; Jang, Y.; Hyeon, T. Synthesis of Monodisperse Spherical Nanocrystals. *Angew. Chem., Int. Ed.* **2007**, *46*, 4630–4660.
11. Xia, Y.; Xiong, Y.; Lim, B.; Skrabalak, S.E. Shape-Controlled Synthesis of Metal Nanocrystals: Simple Chemistry Meets Complex Physics? *Angew. Chem. Int. Ed.* **2009**, *48*, 60–103.
12. Yin, X.; Shi, M.; Wu, J.; Pan, Y.-T.; Gray, D.L.; Bertke, J.A.; Yang, H. Quantitative Analysis of Different Formation Modes of Pt Nanocrystals Controlled by Ligand Chemistry. *Nano Lett.* **2017**, *17*, 6146–6150.
13. Yu, S.; Zhang, C.; Yang, H. Two-Dimensional Metal Nanostructures: From Theoretical Understanding to Experiment. *Chem. Rev.* **2023**, *123*, 3443–3492.
14. Drake, G.A.; Keating, L.P.; Shim, M. Design Principles of Colloidal Nanorod Heterostructures. *Chem. Rev.* **2023**, *123*, 3761–3789.
15. Grogan, J.M.; Rotkina, L.; Bau, H.H. In-Situ Liquid-Cell Electron Microscopy of Colloid Aggregation and Growth Dynamics. *Phys. Rev. E* **2011**, *83*, 061405.
16. Liao, H.G.; Cui, L.; Whitelam, S.; Zheng, H. Real-Time Imaging of Pt_3Fe Nanorod Growth in Solution. *Science* **2012**, *336*, 1011–1014.
17. Wu, J.; Gao, W.; Yang, H.; Zuo, J.-M. Dissolution Kinetics of Oxidative Etching of Cubic and Icosahedral Platinum Nanoparticles Revealed by in situ Liquid Transmission Electron Microscope. *ACS Nano* **2017**, *11*, 1696–1703.
18. Lyu, Z.; Yao, L.; Chen, W.; Kalutantirige, F.C.; Chen, Q. Electron Microscopy Studies of Soft Nanomaterials. *Chem. Rev.* **2023**, *123*, 4051–4145.
19. Kim, B.H.; Yang, J.; Lee, D.; Choi, B.K.; Hyeon, T.; Park, J. Liquid-Phase Transmission Electron Microscopy for Studying Colloidal Inorganic Nanoparticles. *Adv. Mater.* **2018**, *30*, 1703316.
20. Kim, B.H.; Heo, J.; Kim, S.; Reboul, C.F.; Chun, H.; Kang, D.; Bae, H.; Hyun, H.; Lim, J.; Lee, H.; et al. Critical Differences in 3D Atomic Structure of Individual Ligand-Protected Nanocrystals in Solution. *Science* **2020**, *368*, 60–67.
21. Ngo, T.; Yang, H. Toward Ending the Guessing Game: Study of the Formation of Nanostructures Using In Situ Liquid Transmission Electron Microscopy. *J. Phys. Chem. Lett.* **2015**, *6*, 5051–5061.
22. Hodnik, N.; Dehm, G.; Mayrhofer, K.J.J. Importance and Challenges of Electrochemical in Situ Liquid Cell Electron Microscopy for Energy Conversion Research. *Acc. Chem. Res.* **2016**, *49*, 2015–2022.
23. Ross, F.M. Opportunities and Challenges in Liquid Cell Electron Microscopy. *Science* **2015**, *350*, aaa9886.
24. Peng, X.; Shangguan, J.; Zhang, Q.; Hauwiller, M.; Yu, H.; Nie, Y.; Bustillo, K.C.; Alivisatos, A.P.; Asta, M.; Zheng, H. Unveiling Corrosion Pathways of Sn Nanocrystals through High-Resolution Liquid Cell Electron Microscopy. *Nano Lett.* **2024**, *24*, 1168–1175.

25. Zheng, H.; Smith, R.K.; Jun, Y.W.; Kisielowski, C.; Dahmen, U.; Alivisatos, A.P. Observation of Single Colloidal Platinum Nanocrystal Growth Trajectories. *Science* **2009**, *324*, 1309–1312.
26. Zhang, Q.; Peng, X.; Nie, Y.; Zheng, Q.; Shangguan, J.; Zhu, C.; Bustillo, K.C.; Ercius, P.; Wang, L.; Limmer, D.T.; et al. Defect-Mediated Ripening of Core-Shell Nanostructures. *Nat. Commun.* **2022**, *13*, 2211.
27. Zheng, L.; Zhang, X.; Bustillo, K.C.; Yao, Y.; Zhao, L.; Zhu, M.; Li, W.; Zheng, H. Growth Mechanism of Core–Shell PtNi–Ni Nanoparticles Using in Situ Transmission Electron Microscopy. *Nanoscale* **2018**, *10*, 11281–11286.
28. Wu, J.; Gao, W.; Wen, J.; Miller, D.J.; Lu, P.; Zuo, J.-M.; Yang, H. Growth of Au on Pt Icosahedral Nanoparticles Revealed by Low-Dose In Situ TEM. *Nano Lett.* **2015**, *15*, 2711–2715.
29. Zheng, L.; Zhao, L.; Zhao, S.; Zhang, X.; Bustillo, K.C.; Yao, Y.; Yi, X.; Zhu, M.; Li, W.; Zheng, H. A Unique Pathway of PtNi Nanoparticle Formation Observed with Liquid Cell Transmission Electron Microscopy. *Nanoscale* **2020**, *12*, 1414–1418.
30. Li, D.; Nielsen, M.H.; Lee, J.R.I.; Frandsen, C.; Banfield, J.F.; De Yoreo, J.J. Direction-Specific Interactions Control Crystal Growth by Oriented Attachment. *Science* **2012**, *336*, 1014–1018.
31. Welch, D.A.; Woehl, T.J.; Park, C.; Faller, R.; Evans, J.E.; Browning, N.D. Understanding the Role of Solvation Forces on the Preferential Attachment of Nanoparticles in Liquid. *ACS Nano* **2015**, *10*, 181–187.
32. Wang, Y.; Peng, X.; Abelson, A.; Zhang, B.-K.; Qian, C.; Ercius, P.; Wang, L.-W.; Law, M.; Zheng, H. In Situ TEM Observation of Neck Formation During Oriented Attachment of PbSe Nanocrystals. *Nano Res.* **2019**, *12*, 2549–2553.
33. Zhu, C.; Liang, S.; Song, E.; Zhou, Y.; Wang, W.; Shan, F.; Shi, Y.; Hao, C.; Yin, K.; Zhang, T.; et al. *In-Situ* Liquid Cell Transmission Electron Microscopy Investigation on Oriented Attachment of Gold Nanoparticles. *Nat. Commun.* **2018**, *9*, 421.
34. Luo, B.; Smith, J.W.; Ou, Z.; Chen, Q. Quantifying the Self-Assembly Behavior of Anisotropic Nanoparticles Using Liquid-Phase Transmission Electron Microscopy. *Acc. Chem. Res.* **2017**, *50*, 1125–1133.
35. Kim, A.; Akkunuri, K.; Qian, C.; Yao, L.; Sun, K.; Chen, Z.; Vo, T.; Chen, Q. Direct Imaging of "Patch-Clasping" and Relaxation in Robust and Flexible Nanoparticle Assemblies. *ACS Nano* **2024**, *18*, 939–950.
36. Park, J.; Zheng, H.; Lee, W.C.; Geissler, P.L.; Rabani, E.; Alivisatos, A.P. Direct Observation of Nanoparticle Superlattice Formation by Using Liquid Cell Transmission Electron Microscopy. *ACS Nano* **2012**, *6*, 2078–2085.
37. Ou, Z.; Yao, L.; An, H.; Shen, B.; Chen, Q. Imaging How Thermal Capillary Waves and Anisotropic Interfacial Stiffness Shape Nanoparticle Supracrystals. *Nat. Commun.* **2020**, *11*, 4555.
38. Chen, Q.; Yuk, J.M.; Hauwiller, M.R.; Park, J.; Dae, K.S.; Kim, J.S.; Alivisatos, A.P. Nucleation, Growth, and Superlattice Formation of Nanocrystals Observed in Liquid Cell Transmission Electron Microscopy. *MRS Bull.* **2020**, *45*, 713–726.
39. Son, Y.; Kim, B.H.; Choi, B.K.; Luo, Z.; Kim, J.; Kim, G.-H.; Park, S.-J.; Hyeon, T.; Mehraeen, S.; Park, J. In Situ Liquid Phase TEM of Nanoparticle Formation and Diffusion in a Phase-Separated Medium. *ACS Appl. Mater. Interfaces* **2022**, *14*, 22810–22817.
40. Hong, J.; Bae, J.-H.; Jo, H.; Park, H.-Y.; Lee, S.; Hong, S.J.; Chun, H.; Cho, M.K.; Kim, J.; Kim, J.; et al. Metastable Hexagonal Close-Packed Palladium Hydride in Liquid Cell TEM. *Nature* **2022**, *603*, 631–636.
41. Crook, M.F.; Laube, C.; Moreno-Hernandez, I.A.; Kahnt, A.; Zahn, S.; Ondry, J.C.; Liu, A.; Alivisatos, A.P. Elucidating the Role of Halides and Iron during Radiolysis-Driven Oxidative Etching of Gold Nanocrystals Using Liquid Cell Transmission Electron Microscopy and Pulse Radiolysis. *J. Am. Chem. Soc.* **2021**, *143*, 11703–11713.
42. Hauwiller, M.R.; Ye, X.; Jones, M.R.; Chan, C.M.; Calvin, J.J.; Crook, M.F.; Zheng, H.; Alivisatos, A.P. Tracking the Effects of Ligands on Oxidative Etching of Gold Nanorods in Graphene Liquid Cell Electron Microscopy. *ACS Nano* **2020**, *14*, 10239–10250.
43. Woehl, T.J.; Park, C.; Evans, J.E.; Arslan, I.; Ristenpart, W.D.; Browning, N.D. Direct Observation of Aggregative Nanoparticle Growth: Kinetic Modeling of the Size Distribution and Growth Rate. *Nano Lett.* **2014**, *14*, 373–378.
44. Qin, F.; Wang, Z.; Wang, Z.L. Anomalous Growth and Coalescence Dynamics of Hybrid Perovskite Nanoparticles Observed by Liquid-Cell Transmission Electron Microscopy. *ACS Nano* **2016**, *10*, 9787–9793.
45. Talapin, D.V.; Rogach, A.L.; Haase, M.; Weller, H. Evolution of an Ensemble of Nanoparticles in a Colloidal Solution: Theoretical Study. *J. Mater. Chem. B* **2001**, *105*, 12278–12285.
46. Kang, S.; Kim, J.-H.; Lee, M.; Yu, J.W.; Kim, J.; Kang, D.; Baek, H.; Bae, Y.; Kim, B.H.; Kang, S.; et al. Real-Space Imaging of Nanoparticle Transport and Interaction Dynamics by Graphene Liquid Cell TEM. *Sci. Adv.* **2021**, *7*, eabi5419.
47. Kim, J.; Kang, D.; Kang, S.; Kim, B.H.; Park, J. Coalescence Dynamics of Platinum Group Metal Nanoparticles Revealed by Liquid-Phase Transmission Electron Microscopy. *iScience* **2022**, *25*, 104699.
48. Ma, X.; Lin, F.; Chen, X.; Jin, C. Unveiling Growth Pathways of Multiply Twinned Gold Nanoparticles by In Situ Liquid Cell Transmission Electron Microscopy. *ACS Nano* **2020**, *14*, 9594–9604.
49. Ma, X.; Lin, F.; Chen, X.; Jin, C. Synergy between Structure Characteristics and the Solution Chemistry in a Near/Non-Equilibrium Oxidative Etching of Penta-Twinned Palladium Nanorods. *J. Phys. Chem. C* **2021**, *125*, 4010–4020.

50. Zhang, Y.; Keller, D.; Rossell, M.D.; Erni, R. Formation of Au Nanoparticles in Liquid Cell Transmission Electron Microscopy: From a Systematic Study to Engineered Nanostructures. *Chem. Mater.* **2017**, *29*, 10518–10525.
51. Choi, B.K.; Kim, J.; Luo, Z.; Kim, J.; Kim, J.H.; Hyeon, T.; Mehraeen, S.; Park, S.; Park, J. Shape Transformation Mechanism of Gold Nanoplates. *ACS Nano* **2023**, *17*, 2007–2018.
52. Schneider, N.M.; Norton, M.M.; Mendel, B.J.; Grogan, J.M.; Ross, F.M.; Bau, H.H. Electron–Water Interactions and Implications for Liquid Cell Electron Microscopy. *J. Phys. Chem. C* **2014**, *118*, 22373–22382.
53. Woehl, T.J.; Moser, T.; Evans, J.E.; Ross, F.M. Electron-Beam-Driven Chemical Processes During Liquid Phase Transmission Electron Microscopy. *MRS Bull.* **2020**, *45*, 746–753.
54. Lifshitz, I.M.; Slyozov, V.V. The Kinetics of Precipitation from Supersaturated Solid Solutions. *J. Phys. Chem. Solids* **1961**, *19*, 35–50.
55. Viswanatha, R.; Sapra, S.; Satpati, B.; Satyam, P.V.; Dev, B.N.; Sarma, D.D. Understanding the Quantum Size Effects in ZnO Nanocrystals. *J. Mater. Chem.* **2004**, *14*, 661–668.
56. Sholl, D.S.; Skodje, R.T. Late-Stage Coarsening of Adlayers by Dynamic Cluster Coalescence. *Phys. A* **1996**, *231*, 631–647.
57. Meakin, P. Diffusion-Limited Droplet Coalescence. *Phys. A* **1990**, *165*, 1–18.
58. Viswanatha, R.; Sarma, D. D. Growth of Nanocrystals in Solution. In *Nanomaterials Chemistry: Recent Developments and New Directions*; Rao, C.N.R., Müller, A., Cheetham, A.K., Eds.; Verlag GmbH & Co. KGaA: Weinheim, Germany, 2007; pp. 139–170.